Check for updates

View Article Online
View Journal

Chemical Science

Accepted Manuscript

This article can be cited before page numbers have been issued, to do this please use: F. Li, H. Lin, C. Chen, L. Tan, D. Wang, C. Zhao, L. Zhang and C. Su, *Chem. Sci.*, 2026, DOI: 10.1039/D6SC01645F.

Chemical Science

Volume 9
Number 1
7 January 2018
Pages 1-268

rsc.li/chemical-science

ISSN 2041-6539

ROYAL SOCIETY OF CHEMISTRY

EDGE ARTICLE
Xinjing Tang *et al.*
Caged circular siRNAs for photomodulation of gene expression in cells and mice

This is an Accepted Manuscript, which has been through the Royal Society of Chemistry peer review process and has been accepted for publication.

Accepted Manuscripts are published online shortly after acceptance, before technical editing, formatting and proof reading. Using this free service, authors can make their results available to the community, in citable form, before we publish the edited article. We will replace this Accepted Manuscript with the edited and formatted Advance Article as soon as it is available.

You can find more information about Accepted Manuscripts in the Information for Authors.

Please note that technical editing may introduce minor changes to the text and/or graphics, which may alter content. The journal's standard Terms & Conditions and the Ethical guidelines still apply. In no event shall the Royal Society of Chemistry be held responsible for any errors or omissions in this Accepted Manuscript or any consequences arising from the use of any information it contains.

ROYAL SOCIETY OF CHEMISTRY

rsc.li/chemical-science

View Article Online
DOI: 10.1039/D6SC01645F

Journal Name

ARTICLE

Engineering Hydrophobic Covalent Organic Frameworks for Electroreduction of Nitrate to Ammonia

Received 00th July 20xx,
Accepted 00th July 20xx

DOI: 10.1039/x0xx00000x

www.rsc.org/

Fuzhen Li[a], Huan Lin[c], Chunying Chen[c], Li-Lin Tan[b], Dawei Wang[c], Cunyuan Zhao[c], Li Zhang[c],*, Cheng-Yong Su[c]

The development of efficient electrocatalysts for the nitrate reduction reaction (NO_3RR) to ammonia is crucial for sustainable nitrogen management, but remains challenging due to intricate multi-step mechanism and competing side reactions. A key bottleneck is the severe imbalance between the generation and consumption of H*, which critically constrains ammonia selectivity and yield. Herein, a molecular engineering strategy was developed, through the implantation of Pd-porphyrin to promote the generation of H* and meanwhile the graft of ethoxyphenyl groups to create hydrophobic microenvironment and inhibit hydrogen evolution reaction. The covalent organic framework of Pd-PCOF-2(Cu_3), which was prepared from the reaction of Pd(II) diaminoporphyrin and trinuclear copper cluster aldehyde, achieved a high NH_3 Faradaic efficiency of 94.7% and rate of 15.09 $mg \cdot h^{-1} \cdot cm^{-2}$. A rechargeable Zn-$NO_3^-$ battery with Pd-PCOF-2(Cu_3) as the cathode was further constructed, which served as a dual-function system for both power output and ammonia production.

Introduction

Ammonia (NH_3) is a pivotal chemical commodity in modern society, which serves not only as the fundamental feedstock for the fertilizer industry but is also regarded as a promising future energy carrier due to its high energy density and carbon-free nature.[1,2] Currently, industrial ammonia synthesis still predominantly relies on the conventional Haber-Bosch process with harsh conditions of high temperature (350-550 °C) and high pressure (15-25 MPa), which is associated with substantial energy consumption, significant carbon emissions and a deep reliance on fossil fuels, starkly contradicting the global "carbon neutrality" goal.[3] In this context, the direct electrochemical reduction of atmospheric nitrogen (NRR) to ammonia, utilizing renewable electricity and water as the proton source, has garnered significant research interest due to its mild operating conditions and environmentally friendly characteristics. However, its practical application is severely limited by the extremely high dissociation energy of the N≡N triple bond (941 $kJ \cdot mol^{-1}$) and the low solubility of N_2 in aqueous solutions (~0.6 mM), resulting in poor reaction kinetics and negligible yield.[4,5]

Inspired by the comparatively lower dissociation energy of NO_3^- (204 $kJ \cdot mol^{-1}$) and its high solubility, the formation of NH_3 from the electrocatalytic nitrate reduction reaction (NO_3RR) has emerged as a compelling alternative strategy.[6-8] Nevertheless, the NO_3RR process involves a complex multi-step mechanism encompassing an eight-electron, nine-proton transfer pathway ($NO_3^- + 9H^+ + 8e^- \rightarrow NH_3 + 3H_2O$), with the sequential hydrogenation/deoxygenation step of NO_3^- and critical intermediates such as nitrite (NO_2^-) driven by active hydrogen (H*) from H_2O decomposition/reduction.[9,10] Hence, the supply and utilization of H* play a pivotal role.[11,12] An inadequate supply of H* can kinetically limit the hydrogenation steps, leading to the accumulation of reaction intermediates and reduced efficiency. Conversely, an over-abundance of H* readily promotes H–H coupling, triggers the competing hydrogen evolution reaction (HER) and lowers the Faradaic efficiency for NH_3. Therefore, the precise regulation of the H* supply to couple with the specific hydrogenation steps of the nitrate reduction pathway is crucial for achieving optimal performance.[13,14] Some strategies to address this issue have been reported, including single-atom alloys, dual-atom catalysts and heterojunction engineering.[15-20] Given that hydrophobicity can limit the accumulation of water molecules at the catalyst surface and thus suppress HER, the rational construction of a hydrophobic microenvironment to precisely regulate the supply of H* represents a feasible strategy.[21] So far, its application in the field of electrocatalytic NO_3RR has been underdeveloped.

Owing to the precise structural tunability and robust covalent architectures, covalent organic frameworks (COFs)

---

[a] *School of Chemical Engineering and Technology, Sun Yat-sen University, Zhuhai 519082, China.*
[b] *Shantou Engineering Technology Research Center for Green and Precise Manufacturing of High-value Chemicals, Chemistry and Chemical Engineering Guangdong Laboratory, Shantou 515031, China.*
[c] *Lehn Institute of Functional Materials, School of Chemistry, Sun Yat-Sen University, Guangzhou 510006, China; E-mail: zhli99@mail.sysu.edu.cn*

† Electronic Supplementary Information (ESI) includes these details: general information, comparison of electrocatalytic NO_3RR performances of different materials, synthese and charaterizations of PCOFs and electrocatalytic performances. See DOI: 10.1039/x0xx00000x

View Article Online
DOI: 10.1039/D6SC01645E

displayed advantages in electrocatalytic reactions, especially in alkaline conditions.[22-28] Porphyrins possess conjugated structures and excellent electrical properties, and are thus employed as pivotal building blocks and active sites in the construction of porphyrin-based COFs (PCOFs) for electrocatalytic applications.[29-35] Furthermore, the single-metal site within the metallporphyrin is pivotal for the formation of M−H (metal-hydride) active species, which could assist in the electrocatalytic reduction of NO_3^- to NH_3.[36,37] Nevertheless, the vast majority of reported PCOFs are structurally limited to *sql* topology derived from C_4-symmetric tetraphenylporphyrin building blocks. Consequently, not only the promising strategy of porphyrin side-chain engineering for PCOFs remains largely unexplored, but also the design and construction of new PCOF topology merit further investigation.

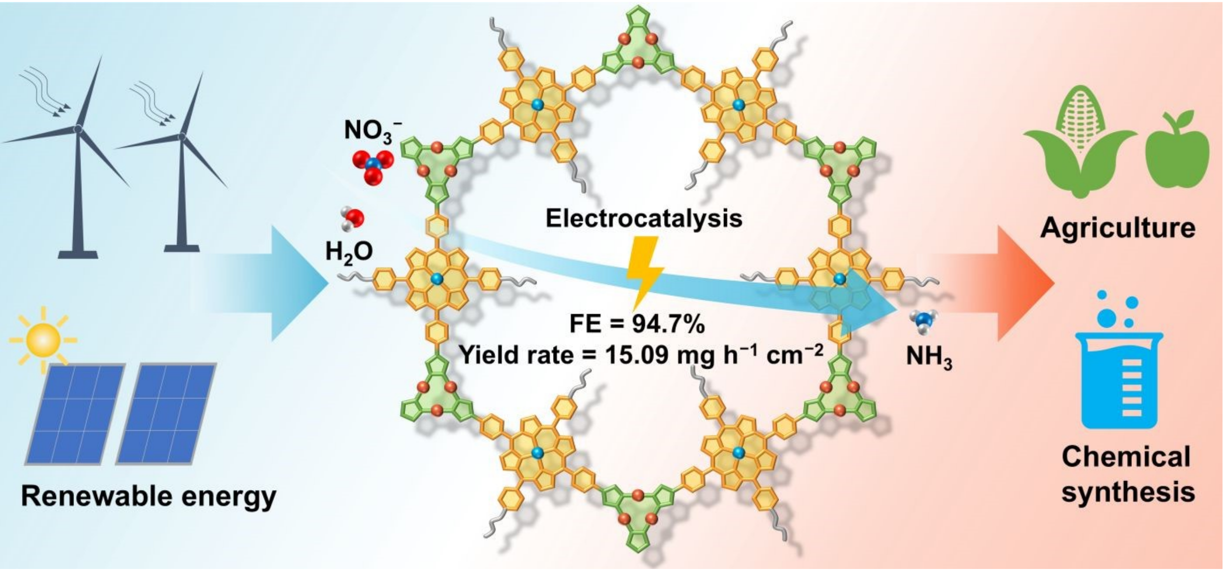

Figure 1. Schematic illustration of electrocatalytic NO_3RR by Pd-PCOF-2(Cu_3).

Herein, three new A_2B_2-type diaminoporphyrin monomers were designed and synthesized, which subsequently reacted with a trinuclear copper cluster (Cu_3) aldehyde ligand via Schiff-base condensation, giving rise to three two-dimensional imine-linked PCOFs with ABC stacking and a hcb topology, denoted as Pd-PCOF-1(Cu_3), Pd-PCOF-2(Cu_3), and PCOF-2(Cu_3), respectively. On one hand, the precise integration of hydrophobic phenyl or ethoxyphenyl side groups of porphyrins engineered a pore-confined hydrophobic microenvironment. On the other hand, the introduction of Pd centers within the porphyrin macrocycles, alongside the Cu_3, established well-defined bimetallic active sites. This deliberate architectural design facilitated exceptional electrocatalytic performance for the NO_3RR under alkaline conditions. Catalytic results showed that Pd-PCOF-2(Cu_3) achieved a remarkable Faradaic efficiency up to 94.7% and a high NH_3 generation rate of 15.09 mg·h^{-1}·cm^{-2} at applied potentials of -1.0 V and -1.1 V vs. RHE, respectively, and maintained stable performances over 10 consecutive catalytic cycles, which ranked top among the reported COFs/MOFs-based electrocatalysts (Table S1). Mechanistic investigations revealed that the hydrophobic microenvironment played a critical role in precisely regulating the supply of H*, which could effectively suppress the competing HER. Concurrently, the Cu_3 and Pd centers served as the catalytic sites for the adsorption/activation of NO_3^- and the hydrogenation of the NO_2^- intermediate, respectively, forming an efficient bimetallic synergistic catalytic mechanism, which minimized the accumulation of NO_2^-, enhanced the overall reaction rate, and optimized NO_3^- to NH_3 conversion (Figure 1).

Experimental

Synthesis of 5,15-diphenyl-10,20-bis(4-nitrophenyl) porphyrin (DNPP). Prior to the synthesis of DNPP, 2,2'-((4-nitrophenyl)methylene)bis(1H-pyrrole) (NPBPR) was prepared (Figures S1 and S2). And then, NPBPR (5.34 g, 0.02 mol), benzaldehyde (2.12 g, 0.02 mol) and propionic acid (300 mL) were mixed in a 500 mL round-bottom flask. The mixture was stirred at 140 °C for 2 h and then cooled down to room temperature. After propionic acid was removed under reduced pressure, the crude product was purified by column chromatography (silica, CH_2Cl_2/MeOH 49:1) to afford DNPP as purple solid (0.78 g, 11% yield).

Synthesis of 5,15-bis(4-ethoxyphenyl)-10,20-bis(4-nitrophenyl)porphyrin (EDNPP). EDNPP was synthesized using the similar procedure as that of DNPP except that benzaldehyde was replaced by 4-ethoxybenzaldehyde (3.0 g, 0.02 mol). EDNPP was obtained as purple solid (0.95 g, 12% yield).

Synthesis of 5,15-bis(4-ethoxyphenyl)-10,20-bis(4-aminophenyl)porphyrin (EDAPP). EDNPP (0.317 g, 0.4 mmol), stannous chloride dihydrate ($SnCl_2·2H_2O$, 0.36 g, 1.6 mmol), tetrahydrofuran (THF, 70 mL) and concentrated hydrochloric

View Article Online
DOI: 10.1039/D6SC01645F

acid (HCl, 10 mL) were mixed in a 250 mL round-bottom flask. The mixture was stirred at 70 °C for 2 h and then cooled down to room temperature. After the excess HCl was neutralized with ammonia water, the mixture was extracted with CH_2Cl_2. The organic layer was collected, dried over Na_2SO_4 and concentrated under reduced pressure. Subsequently, the crude product was purified by column chromatography (silica, CH_2Cl_2/MeOH 49:1) to afford EDAPP as purple solid (0.264 g, 90% yield). ^{1}H NMR (400 MHz, DMSO-d_6, Figure S3) δ 8.92 (d, J = 4.8 Hz, 4H), 8.82 (d, J = 4.8 Hz, 4H), 8.11 (d, J = 8.4 Hz, 4H), 7.85 (d, J = 8.1 Hz, 4H), 7.37 (d, J = 8.5 Hz, 4H), 7.01 (d, J = 8.3 Hz, 4H), 5.57 (s, 4H), 4.35 (q, J = 6.9 Hz, 4H), 1.54 (t, J = 6.9 Hz, 6H), -2.79 (s, 2H).

Synthesis of Pd(II)-5,15-diphenyl-10,20-bis(4-nitrophenyl)porphyrin (Pd-DNPP). DNPP (0.35 g, 0.5 mmol), palladium chloride ($PdCl_2$, 0.35 g, 2 mmol) and DMF (200 mL) were mixed in a 500 mL round-bottom flask. The mixture was stirred at 160 °C for 12 h and then cooled down to room temperature. After DMF was removed under reduced pressure, the crude product was purified by column chromatography (silica, CH_2Cl_2/MeOH 49:1) to afford Pd-DNPP as reddish purple solid (0.364 g, 90% yield).

Synthesis of Pd(II)-5,15-bis(4-ethoxyphenyl)-10,20-bis(4-nitrophenyl)porphyrin (Pd-EDNPP). Pd-EDNPP was synthesized using the similar procedure as that of Pd-DNPP except that DNPP was replaced by EDNPP (0.396 g, 0.5 mmol). Pd-EDNPP was obtained as reddish purple solid (0.412 g, 92% yield).

Synthesis of Pd(II)-5,15-diphenyl-10,20-bis(4-aminophenyl)porphyrin (Pd-DAPP). Pd-DAPP was synthesized using the similar procedure as that of EDAPP except that EDNPP was replaced by Pd-DNPP (0.32 g, 0.4 mmol). Pd-DAPP was obtained as reddish purple solid (0.282 g, 94% yield). ^{1}H NMR (400 MHz, DMSO-d_6, Figure S4) δ 8.93 (d, J = 5.0 Hz, 4H), 8.75 (d, J = 4.9 Hz, 4H), 8.18 (d, J = 5.2 Hz, 4H), 7.92 - 7.73 (m, 10H), 6.99 (d, J = 8.0 Hz, 4H), 5.56 (s, 4H).

Synthesis of Pd(II)-5,15-bis(4-ethoxyphenyl)-10,20-bis(4-aminophenyl)porphyrin (Pd-EDAPP). Pd-EDAPP was synthesized using the similar procedure as that of Pd-DAPP except that Pd-DNPP was replaced by Pd-EDNPP (0.358 g, 0.4 mmol). Pd-EDAPP was obtained as reddish purple solid (0.295 g, 88% yield). ^{1}H NMR (400 MHz, DMSO-d_6, Figure S5) δ 8.92 (d, J = 4.9 Hz, 4H), 8.81 (d, J = 5.0 Hz, 4H), 8.08 (d, J = 8.4 Hz, 4H), 7.81 (d, J = 8.1 Hz, 4H), 7.36 (d, J = 8.3 Hz, 4H), 7.00 (d, J = 8.2 Hz, 4H), 5.58 (s, 4H), 4.35 (q, J = 7.1 Hz, 4H), 1.55 (t, J = 6.9 Hz, 6H).

Synthesis of Pd-PCOF-1(Cu_3). Pd-DAPP (22.47 mg, 0.03 mmol), $Cu_3(PyCA)_3$ (9.52 mg, 0.02 mmol), *n*-butanol (*n*-BuOH, 0.5 mL) and *o*-dichlorobenzene (*o*-DCB, 0.5 mL) were sequentially added to a 10 mL Schlenk tube and sonicated for 5 min. Subsequently, TFA (6 M, 0.1 mL) was added to the tube and sonicated for 5 min, and then the tube was degassed and heated at 120 °C for 3 days. The precipitated solid was collected by centrifugation and washed sequentially with THF, DMF and acetone several times. The solids were dried at 100 °C for 12 h to afford Pd-PCOF-1(Cu_3) (27 mg, 85% yield) as red powders.

Synthesis of Pd-PCOF-2(Cu_3) and PCOF-2(Cu_3). The synthesis procedure for Pd-PCOF-2(Cu_3) and PCOF-2(Cu_3) was similar to that of Pd-PCOF-1(Cu_3) except that Pd-EDAPP and EDAPP were used instead of Pd-DAPP. Pd-PCOF-2(Cu_3) (30 mg, 86% yield) and PCOF-2(Cu_3) (22.3 mg, 71% yield) were obtained as red and brown powders, respectively.

Electrochemical measurements. To prepare the working electrodes, 10 mg of the as-prepared catalyst, 5 mg of acetylene black, and 50 μL of Nafion solution (5 wt%) were dispersed in 450 μL of isopropanol (IPA) and sonicated for 30 min to give a homogeneous catalyst ink. Subsequently, 50 μL of the catalyst ink was dropped on a hydrophobic carbon cloth with an area of 1 cm^2 (the area of carbon cloth was 1 × 2 cm^2) and dried at 80℃ for 1 h to achieve a catalyst areal loading of 1 mg·cm^{-2}. The electrochemical NO_3RR measurements were carried out with a standard three-electrode system using a typical H-type electrolytic cell separated by a Nafion 117 membrane at room temperature and atmospheric pressure. The H-cell was conducted on a CHI 660E workstation (Shanghai Chenhua), and equipped with Platinum plate counter electrode and Hg/HgO (with 1 M KOH solution) reference electrode. All the potentials in the measurements were transformed against reversible hydrogen electrodes (RHEs) according to Potential = $E_{Hg/HgO}$ + 0.0592 pH + 0.098 V (pH = 14 for 1 M KOH). The electrolyte (60 mL 1 M KOH) was evenly distributed to the cathode and anode compartment and 0.1 M KNO_3 was added only to the cathode compartment. Before the electrochemical measurement, the electrolyte of cathode compartment was purged with 20 sccm of high-purity Ar (99.999%) for 10 min to remove dissolved O_2, and the flow rate of Ar was adjusted to 10 sccm during the measurement. Linear sweep voltammetry (LSV) was collected at a scan rate of 10 mV s^{-1}. The chronoamperometry test was performed at every 0.1 V from -0.6 V to -1.1 V vs. RHE for 1000 s under a constant stirring rate of 800 rpm, and the products (NH_3, NO_2^- and H_2) were determined quantitatively separately. For cycle stability test, the chronoamperometry test was performed at -0.9 V vs. RHE for 1000 s and using the fresh electrolyte for every cycle. Electrochemical impedance spectroscopic (EIS) measurements were performed with 5 mV amplitude over a frequency ranging from 1000000 to 0.1 Hz at 0 V.

Assembly of the Zn-NO_3^- battery and electrochemical test. The Zn-NO_3^- battery was constructed using a typical H-type cell, in which the carbon cloth-supported Cu_3-Pd-PorMCOF-2 (1 × 1 cm^2, catalyst mass loading of 1 mg·cm^{-2}) and Zn plate (2 × 2 cm^2) served as the cathode and anode, respectively. The catholyte (60 mL 1 M KOH + 0.1 M KNO_3) and anolyte (1 M KOH + 0.2 M $Zn(Ac)_2$) were separated by a Nafion 117 membrane. Before electrochemical tests, the catholyte was purged with high-purity Ar (99.999%) for 30 min to remove dissolved O_2. The open-circuit voltage test, discharging polarization curves with a scan rate of 10 mV·s^{-1}, chronoamperometry (i~t) and discharge-charge processes at a constant current density of 1 mA·cm^{-2} were conducted on a

CHI 660E workstation (Shanghai Chenhua) at room temperature. After electrochemical test, the catholyte was collected and the ammonia concentration was measured through the indophenol blue method.

The power density (P) of the Zn-NO_3^- battery was calculated by the following formula:

$$P = I \times V$$

where I and V are the discharge current density and voltage, respectively.

Results and discussion

Synthesis and characterizations. Three new porphyrin ligands such as Pd(II)-5,15-diphenyl-10,20-bis(4-aminophenyl)porphyrin (Pd-DAPP), Pd(II)-5,15-bis(4-ethoxyphenyl)-10,20-bis(4-aminophenyl)porphyrin (Pd-EDAPP) and 5,15-bis(4-ethoxyphenyl)-10,20-bis(4-aminophenyl) porphyrin (EDAPP) were designed and synthesized (Figure S6). The solvothermal reaction of Pd-DAPP, Pd-EDAPP and EDAPP and tris(μ_2-4-carboxaldehyde-pyrazolato-N,N')-tricopper ($Cu_3(PyCA)_3$, Figures S7 and S8) in the presence of 6 M trifluoroacetic acid (TFA) generated three imine bonded covalent organic frameworks named as Pd-PCOF-1(Cu_3), Pd-PCOF-2(Cu_3) and PCOF-2(Cu_3), respectively (Figures 2 and S9-S11). The three PCOFs were predicted to possess well-aligned frameworks with hcb topology, according to the [3+2] ligand combination.

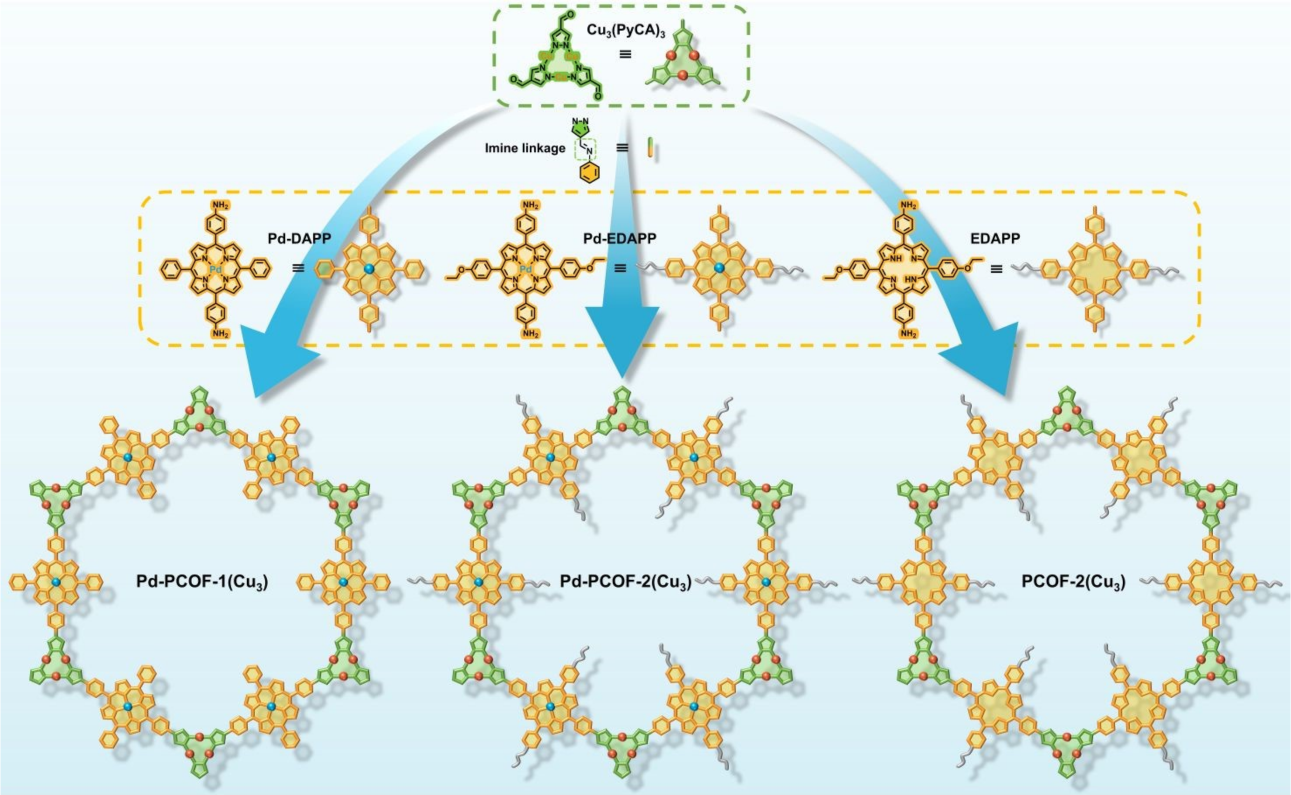

Figure 2. Synthesis of Pd-PCOF-1(Cu_3), Pd-PCOF-2(Cu_3) and PCOF-2(Cu_3).

The crystalline architectures of Pd-PCOF-1(Cu_3), Pd-PCOF-2(Cu_3) and PCOF-2(Cu_3) were determined via powder X-ray diffraction (PXRD) measurement and theoretical structural simulations via Materials Studio (Figure 3a-c). Pd-PCOF-1(Cu_3) exhibited two distinct peaks at 2θ = 3.40° and 6.80°, corresponding to the (110) and (220) planes, respectively (Figure 3d). Pawley refinement gave the optimized unit cell parameters of $a = b$ = 54.020 Å, c = 6.739 Å, $\alpha = \beta$ = 90.00°, γ = 120.00° and good-agreement parameters of R_p = 3.70% and R_{wp} = 3.20% for Pd-PCOF-1(Cu_3) (Tables S2-S4). According to theoretical structure simulations, the experimental PXRD patterns of Pd-PCOF-1(Cu_3) well agreed with the simulated ABC stacking (staggered) model in the R-3 space group rather than AA or AB stacking model (Figures S12 and S13). It is noted that the PXRD patterns of the three PCOFs were different from those of Pd-DAPP, Pd-EDAPP, EDAPP and $Cu_3(PyCA)_3$, demonstrating the formation of the new crystal structures (Figures S14-S16).

Pd-PCOF-2(Cu_3) and PCOF-2(Cu_3) displayed similar PXRD patterns and sharper diffraction peaks than Pd-PCOF-1(Cu_3), indicating that the introduction of the ethyl group significantly improved crystallinity but did not fundamentally alter the structure of ABC stacking model in the R-3 space group (Figures 3e, 3f and S17-20, Tables S5-S10). Taking Pd-PCOF-2(Cu_3) as an example, the PXRD pattern of Pd-PCOF-2(Cu_3) displayed two dominant peaks at 2θ = 3.30° and 6.60° and three weaker peaks at 2θ = 5.76°, 11.44° and 13.20°, which were assigned to the (110), (220), (300), (600), and (440) facet diffractions in the calculated ABC stacking mode, respectively (Figures 3e, S17 and S18). The simulated PXRD curve of ABC

View Article Online
DOI: 10.1039/D6SC01645E

stacking model matched well with the experimental one with small fitting parameters of R_p = 2.37% and R_{wp} = 1.47% and the optimized unit cell parameters were determined to be $a = b$ = 53.903 Å, c = 6.953 Å, $\alpha = \beta$ = 90.00° and γ = 120.00° on the basis of the Pawley refinement (Table S7).

The scanning electron microscope (SEM) and high-resolution transmission electron microscope (HR-TEM) were used to investigate the morphology and crystal structure of these three PCOFs. In the SEM images, the three PCOFs exhibited irregular nanoparticles with a size ranging 100-200 nm (Figures S21-S23). Their HR-TEM images displayed distinct lattice fringes with a spacing of approximately 2.52, 2.62 and 2.58 nm for Pd-PCOF-1(Cu_3), Pd-PCOF-2(Cu_3) and PCOF-2(Cu_3), respectively, corresponding to their (110) facets, which were in good agreement with the theoretical values of 27.02, 26.95 and 27.06 Å based on the ABC stacking model, further proving their high crystallinity (Figure 3g-i).

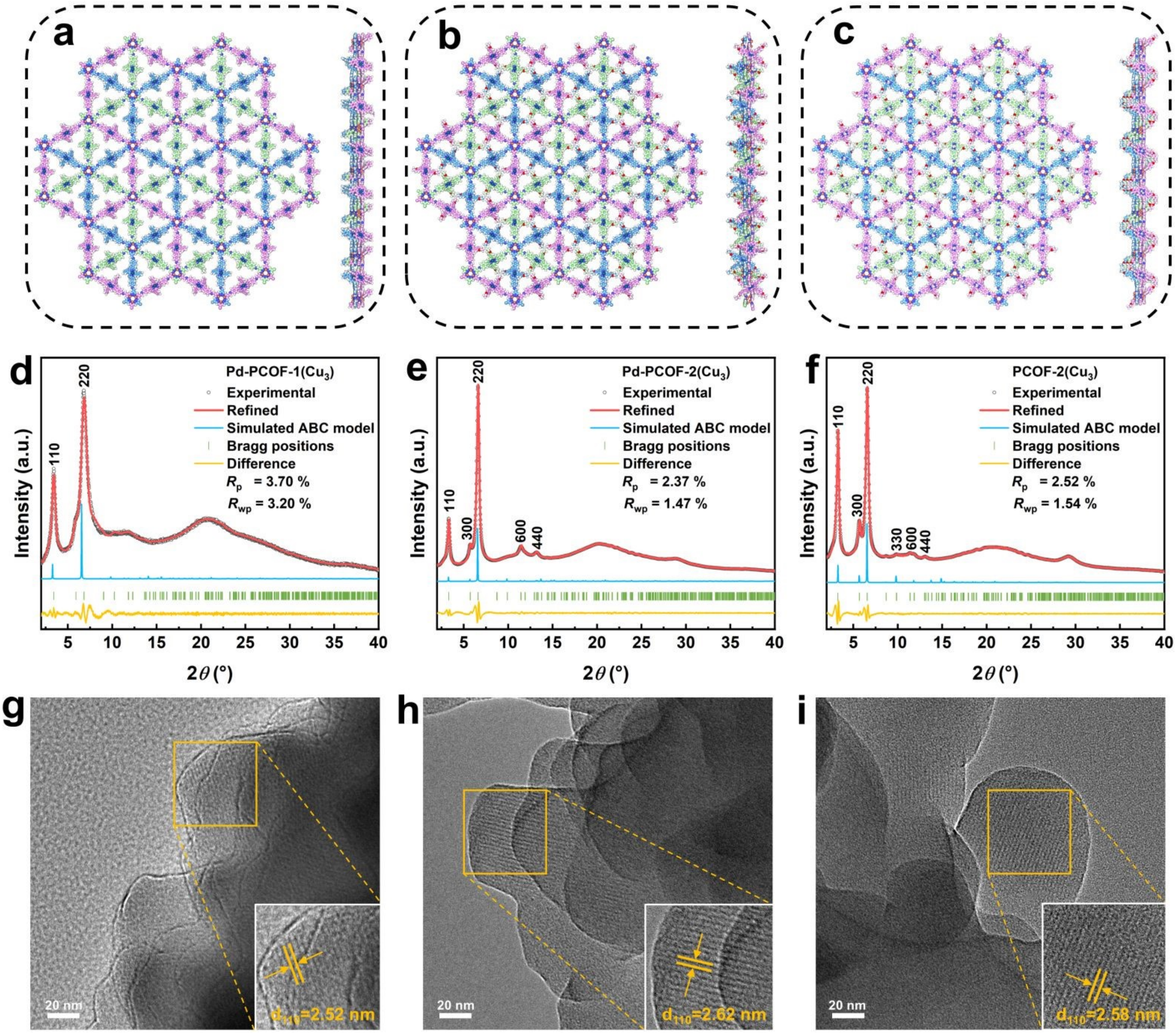

Figure 3. ABC stacking model of Pd-PCOF-1(Cu_3) (a), Pd-PCOF-2(Cu_3) (b) and PCOF-2(Cu_3) (c) viewed from *c* axis (left) and *a* axis (right). PXRD patterns of Pd-PCOF-1(Cu_3) (d), Pd-PCOF-2(Cu_3) (e) and PCOF-2(Cu_3) (f) with the experimental profiles, Pawley refined, difference curve, and simulated profiles of ABC models. HR-TEM images of Pd-PCOF-1(Cu_3) (g), Pd-PCOF-2(Cu_3) (h) and PCOF-2(Cu_3) (i), and the inset were enlarged images of a selective area showing well-ordered lattice fringe of (110).

Fourier transform infrared (FT-IR) spectrometry was employed to analyze the chemical structure of the three PCOFs (Figure 4a). The peak of C=O stretching vibration of $Cu_3(PyCA)_3$ appeared at 1670 cm^{-1}, and meanwhile, the N−H and C=N stretching vibrations of the porphyrin rings were located at 3300-3500 and 1620 cm^{-1}, respectively (Figures S24-26).

View Article Online
DOI: 10.1039/D6SC01645F

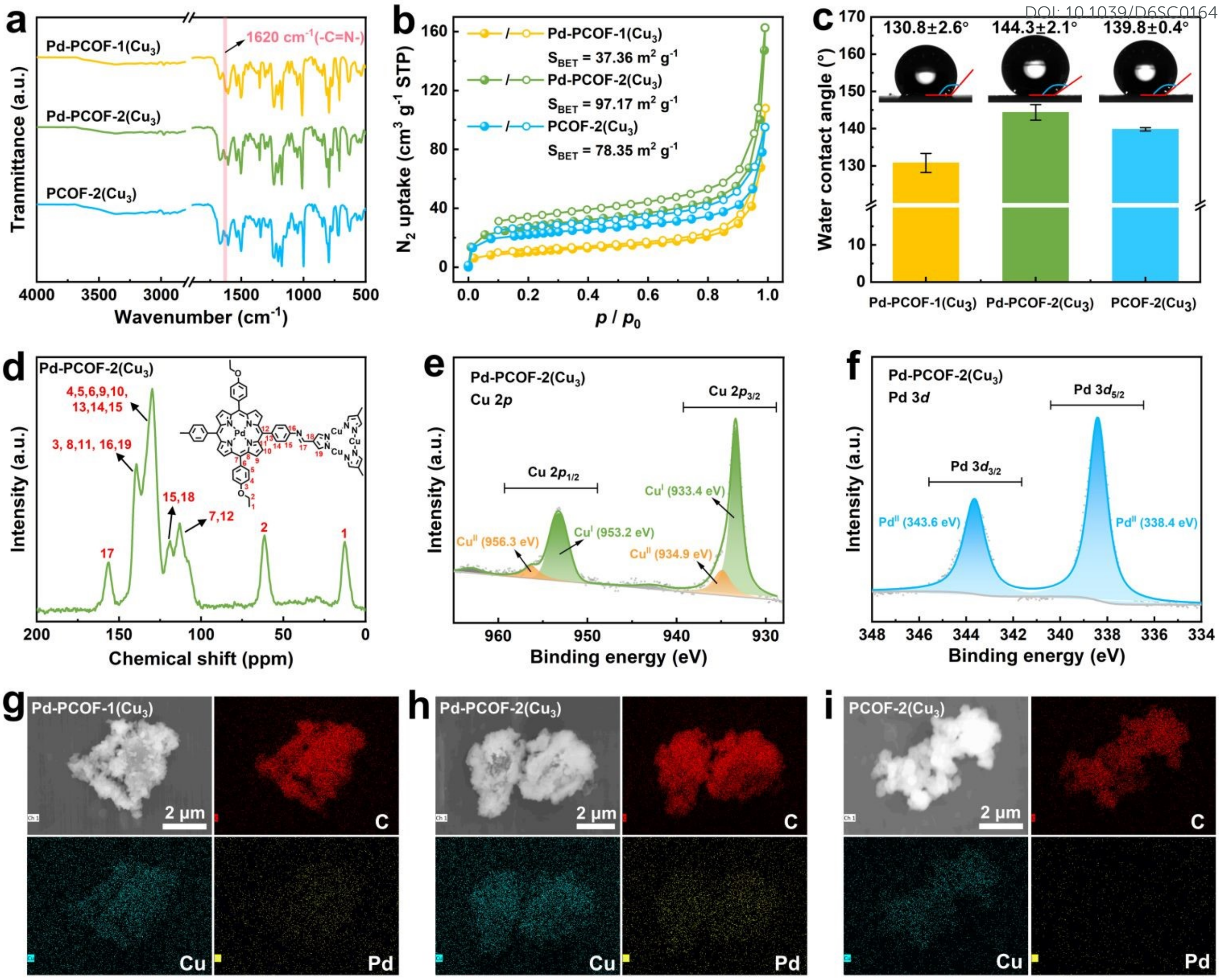

Figure 4. FT-IR spectra (a), N_2 adsorption isotherm curves profiles (b) and water contact angle (c) of PCOFs. Solid-state ^{13}C CP-MAS NMR spectra (d) and XPS spectra of Cu 2*p* (e) and Pd 3*d* (f) for Pd-PCOF-2(Cu$_3$). EDS elemental mappings of PCOF (g-i).

N_2 adsorption-desorption isotherms at 77 K were employed to characterize the porosity of Pd-PCOF-1(Cu$_3$), Pd-PCOF-2(Cu$_3$) and PCOF-2(Cu$_3$) (Figure 4b). All the three COFs exhibited typical type-II reversible isotherms with the Brunauer-Emmett-Teller (BET) surface areas of 37.36, 97.17 and 78.15 m^2 g^{-1} for Pd-PCOF-1(Cu$_3$), Pd-PCOF-2(Cu$_3$) and PCOF-2(Cu$_3$), respectively. The reduced BET surface areas of Pd-PCOF-1(Cu$_3$) may be attributed to its lower crystallinity than Pd-PCOF-2(Cu$_3$) and PCOF-2(Cu$_3$). According to the nonlocal density functional theory (NLDFT) method, the pore sizes were predominantly distributed at approximately 0.93, 0.80, and 0.88 nm for Pd-PCOF-1(Cu$_3$), Pd-PCOF-2(Cu$_3$) and PCOF-2(Cu$_3$), respectively (Figure S27).

According to the static water contact angle measurement, obvious hydrophobicity was visualized in the three PCOFs, in which the water contact angles were measured to be 130.8°, 144.3° and 139.8° for Pd-PCOF-1(Cu$_3$), Pd-PCOF-2(Cu$_3$) and PCOF-2(Cu$_3$), respectively (Figure 4c). Compared with Pd-PCOF-1(Cu$_3$), the increased water contact angle of Pd-PCOF-2(Cu$_3$) and PCOF-2(Cu$_3$) might be attributed to the presence of the ethoxyphenyl groups onto the channels.

Solid-state ^{13}C cross-polarization magic angle spinning nuclear magnetic resonance (^{13}C CP-MAS NMR) spectrum of Pd-PCOF-2(Cu$_3$) was examined. The characteristic C signal of the ethoxy group were observed at 61.5 and 12.5 ppm, while porphyrin ring and pyrazole carbons exhibited resonance at 139.5, 129.5, 118.5 and 113.0 ppm and 139.5 and 118.5 ppm, respectively, in Pd-PCOF-2(Cu$_3$) (Figure 4d). The characteristic resonance peak of the imine carbon appeared at ~156.5 ppm in the ^{13}C CP-MAS NMR spectrum, which further confirmed the successful formation of imine bonds.

The electronic valence state of the PCOFs was investigated by X-ray photoelectron spectroscopy (XPS) measurements. The full XPS spectra of both Pd-PCOF-1(Cu$_3$) and Pd-PCOF-2(Cu$_3$) displayed C 1*s*, N 1*s*, O1*s*, Cu 2*p* and Pd 3*d* elemental signal peaks, while the full XPS spectrum of PCOF-2(Cu$_3$) only showed

View Article Online
DOI: 10.1039/D6SC01645E

C 1*s*, N 1*s*, O1*s* and Cu 2*p* elemental signal peaks (Figure S28). Furthermore, the high-resolution Cu 2*p* XPS spectrum of Pd-PCOF-2(Cu$_3$) showed two major peaks belong to Cu 2$p_{1/2}$ and Cu 2$p_{3/2}$, which were mainly composed of the peaks assigned to the binding energy of Cu^{I} centered at 953.2 and 933.4 eV (Figure 4e). It was similar for Pd-PCOF-1(Cu$_3$) (953.2 and 933.4 eV), PCOF-2(Cu$_3$) (953.1 and 933.2 eV) and Cu$_3$(PyCA)$_3$ (952.8 and 933.0 eV), revealing the main Cu^{I} state nature of the Cu$_3$ moiety (Figure S29). The high-resolution Pd 3*d* XPS spectrum of Pd-EDAPP, Pd-PCOF-1(Cu$_3$) and Pd-PCOF-2(Cu$_3$) all exhibited two peaks centered at 343.6 and 338.4 eV, corresponding to the Pd 3$d_{3/2}$ and Pd 3$d_{5/2}$, respectively, indicating a +2 oxidation state of the coordinated palladium centers in porphyrin (Figures 4f and S30). The results of XPS spectra demonstrated that the formation of PCOFs did not alter the oxidation states of copper and palladium of the starting materials.

Energy-dispersive X-ray (EDS) spectroscopy was employed to investigate elemental distribution, which demonstrated the homogeneous dispersion of C, Cu and Pd within both Pd-PCOF-1(Cu$_3$) and Pd-PCOF-2(Cu$_3$), whilst C and Cu within PCOF-2(Cu$_3$) (Figure 4g-i).

Chemical structural stability of the PCOFs was firstly studied through the thermogravimetric analysis (TGA), which disclosed only 5% mass loss at 265, 244 and 235 °C under the N$_2$ atmosphere for Pd-PCOF-1(Cu$_3$), Pd-PCOF-2(Cu$_3$) and PCOF-2(Cu$_3$), respectively (Figure S31). Furthermore, the PXRD patterns of Pd-PCOF-2(Cu$_3$) and PCOF-2(Cu$_3$) remained almost unchanged after being soaked in a range of solvents such as tetrahydrofuran (THF), acetonitrile (CH$_3$CN), methanol (CH$_3$OH), 1 M NaOH and 0.1 M HCl for 24 h (Figures S32 and S33). Pd-PCOF-1(Cu$_3$) was also stable in these solvents with the exception of 0.1 M HCl (Figure S34). These studies revealed the high chemical structural stability of these PCOFs and the importance of hydrophobicity in the acid-base resistance.

Electrocatalytic performances. Electrocatalytic NO$_3$RR performances of Pd-PCOF-1(Cu$_3$), Pd-PCOF-2(Cu$_3$) and PCOF-2(Cu$_3$) were evaluated in a standard three-electrode H-type cell containing 1 M KOH with 0.1 M KNO$_3$ under room temperature (Figure S35). All potentials were referenced against the RHE without *iR* compensation. ^{1}H NMR measurement and ultraviolet-visible (UV-vis) spectrophotometry based on indophenol blue method were employed to quantify NH$_3$, while UV-vis spectrophotometry based on Griess test and gas chromatographic were used to detect NO$_2^-$ and H$_2$, respectively, in which the calibration curves were presented in Figures S36-S39.

The linear sweep voltammetry (LSV) curves revealed a dramatic enhancement in the current density upon the addition of NO$_3^-$ for the three PCOFs, manifesting their remarkable electrocatalytic NO$_3$RR activity (Figure 5a). Pd-PCOF-1(Cu$_3$) and Pd-PCOF-2(Cu$_3$) displayed stronger current density responses than PCOF-2(Cu$_3$), suggesting that the implantation of Pd centers in porphyrin could improve the NO$_3$RR activity.

The chronoamperometry electrolysis with applied potentials from -0.6 to -1.1 V vs. RHE was employed to investigate the differences in electrocatalytic efficiency among Pd-PCOF-1(Cu$_3$), Pd-PCOF-2(Cu$_3$) and PCOF-2(Cu$_3$) (Figures S40-S42). The NH$_3$ generation rate exhibited a nearly linear enhance with increasingly negative applied potential and reached the maximum value of 14.34 and 15.09 mg·h^{-1}·cm^{-2} at -1.1 V vs. RHE for Pd-PCOF-1(Cu$_3$) and Pd-PCOF-2(Cu$_3$), respectively, which were superior to that of PCOF-2(Cu$_3$) (9.52 mg·h^{-1}·cm^{-2}), further demonstrating the contribution of Pd center in porphyrin to enhance the overall electrocatalytic activity (Figure 5b). The faradaic efficiencies (FEs) of NH$_3$ exhibited a typical volcano-shaped trend (Figure 5c). Pd-PCOF-2(Cu$_3$) maintained the highest NH$_3$ FEs (over 80%) among the three PCOFs at almost all applied potentials and reached the maximum value of 94.70% at -1.0 V vs. RHE, which was significantly higher than those of Pd-PCOF-1(Cu$_3$) (87.69% at -0.9 V vs. RHE) and PCOF-2(Cu$_3$) (86.96% at -0.8 V vs. RHE).

The NO$_2^-$ FEs of all the PCOFs gradually decreased with negative potentials increasing, under which conditions more active hydrogen (H*) could be generated and subsequently promoted the hydrogenation of NO$_2^-$ to NH$_3$, thereby reducing the accumulation of NO$_2^-$ (Figure 5d). For comparison, the H$_2$ FEs increased sharply with negative potentials increasing (Figure 5e). Compared to Pd-PCOF-1(Cu$_3$) and PCOF-2(Cu$_3$), Pd-PCOF-2(Cu$_3$) exhibited much lower H$_2$ FEs at all potentials. It demonstrated not only HER was suppressed by the hydrophobic microenvironment but also the NO$_3$RR process was promoted by the generation of H* of Pd-porphyrin.

Pd-PCOF-2(Cu$_3$) maintained excellent electrocatalytic performance stability for NO$_3$RR at -0.9 V vs. RHE over 10 consecutive cycles, without obvious degradation in FE and generation rate of NH$_3$ (Figure 5f and Figure S43). The PXRD pattern of Pd-PCOF-2(Cu$_3$) after electrocatalysis over 10 consecutive cycles retained characteristic diffraction peaks at 2θ = 3.30° and 6.60° (Figure S44).

In short, owing to the suppression of the competitive HER by the hydrophobic microenvironment and the synergistic catalysis of Cu$_3$ cluster and Pd-porphyrin, Pd-PCOF-2(Cu$_3$) achieved superior electrocatalytic performances for NO$_3$RR with regards to NH$_3$ FEs and generation in comparison with most reported MOFs/COFs-based electrocatalysts (Figure 5g and Table S1).

Reaction mechanism studies. To gain a more in-depth and comprehensive understanding of the reaction mechanism of NO$_3$RR, further investigations were carried out. Firstly, ^{15}N isotopic labeling experiments were performed to identify the origin of nitrogen in the NH$_3$ produced. The ^{1}H NMR spectra of the electrolytes employing ^{14}NO$_3^-$ and ^{15}NO$_3^-$ as N source revealed the typical characteristic triplet peaks of ^{14}NH$_4^+$ (at 6.77, 6.90 and 7.03 ppm) and doublet peaks of ^{15}NH$_4^+$ (at 6.81 and 6.99 ppm), respectively, confirming that NH$_3$ was originated from the electrocatalytic NO$_3$RR (Figures 6a and S45).

View Article Online
DOI: 10.1039/D6SC01645F

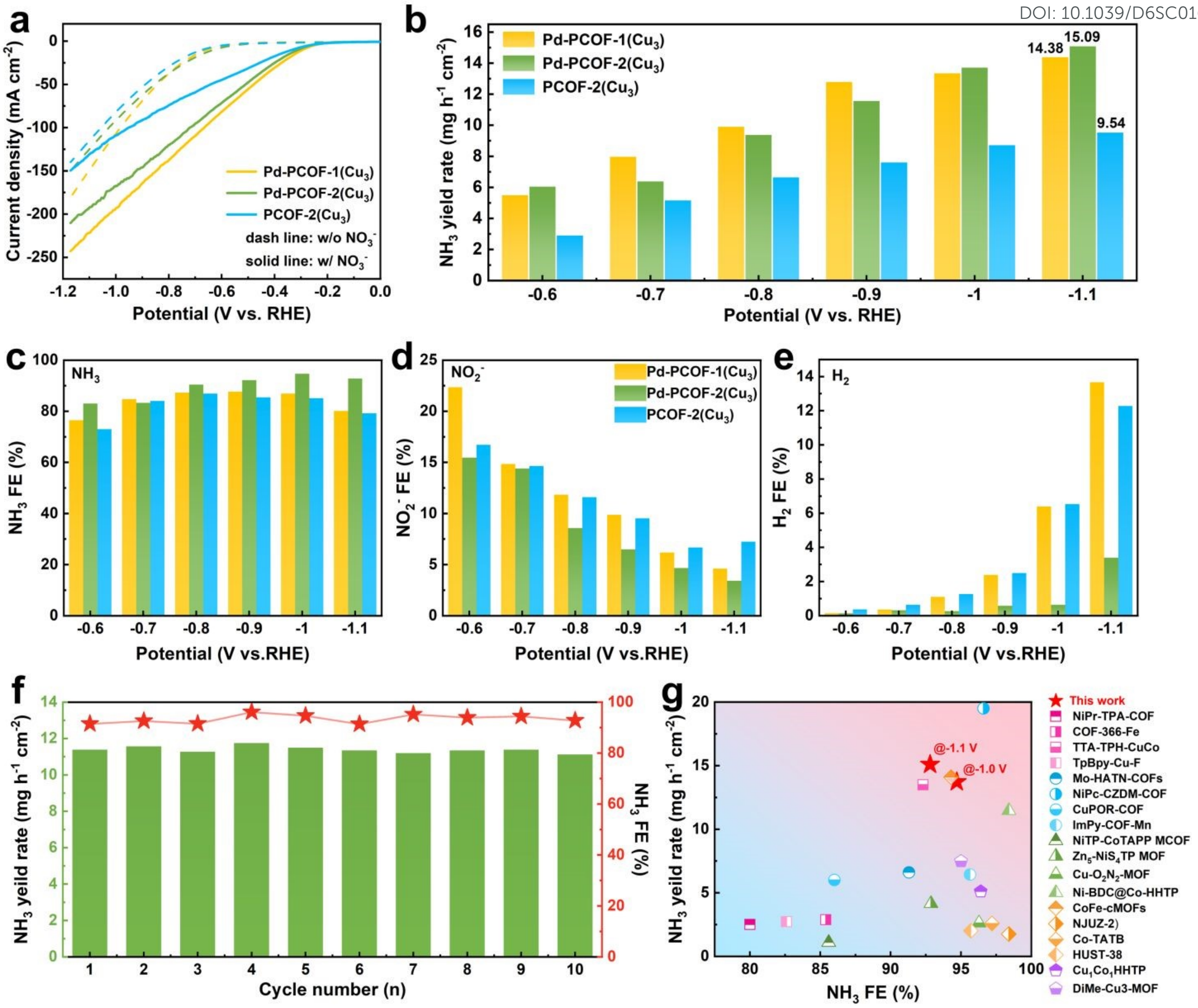

Figure 5. Linear scanning voltammetry (LSV) curves of Pd-PCOF-1(Cu$_3$), Pd-PCOF-2(Cu$_3$) and PCOF-2(Cu$_3$) in 1 M KOH with 0.1 M KNO_3 (solid lines) or without KNO_3 (dash lines) at a scan rate of 10 mV s^{-1} (a). NH_3 yield rate of Pd-PCOF-1(Cu$_3$), Pd-PCOF-2(Cu$_3$) and PCOF-2(Cu$_3$) at different applied potentials (b). NH_3 (c), NO_2^- (d) and H_2 (e) FEs of Pd-PCOF-1(Cu$_3$), Pd-PCOF-2(Cu$_3$) and PCOF-2(Cu$_3$) at different applied potentials. Stability of Pd-PCOF-2(Cu$_3$) for NO_3RR at -0.9 V vs. RHE (f). Comparison of NH_3 yield rate and FE of Pd-PCOF-2(Cu$_3$) with reported MOFs/COFs-based electrocatalysts (Table S1) (g).

Pd-PCOF-2(Cu$_3$) (241 mV·dec^{-1}) and PCOF-2(Cu$_3$) (239 mV·dec^{-1}) manifested higher Tafel slopes than Pd-PCOF-1(Cu$_3$) (217 mV dec^{-1}), revealing an inhibitory effect of the hydrophobic microenvironment on the water dissociation kinetics (Figure 6b). It is noted that the H* generated from water dissociation ($H_2O + M + e^- \rightarrow M{-}H^* + OH^-$) is crucial to the deoxygenation and hydrogenation of NO_3^- and intermediate. With the addition of NO_3^-, Tafel slopes of Pd-PCOF-1(Cu$_3$) and Pd-PCOF-2(Cu$_3$) decreased significantly to 149 and 161 mV·dec^{-1}, respectively, which were lower than that of PCOF-2(Cu$_3$) (222 mV·dec^{-1}), demonstrating that the presence of Pd center in the porphyrin rings enhanced NO_3RR kinetics (Figure 6c). In addition, Pd-porphyrin-based COFs of Pd-PCOF-1(Cu$_3$) (2.4 Ω) and Pd-PCOF-2(Cu$_3$) (2.8 Ω) exhibited lower charge transfer resistance than PCOF-2(Cu$_3$) (3.1 Ω) (Figure S46).

According to LSV curves normalized by electrochemical surface area (ECSA, Figure S47), Pd-PCOF-2(Cu$_3$) presented superior current density responses than Pd-PCOF-1(Cu$_3$) and PCOF-2(Cu$_3$), demonstrating the highest intrinsic NO_3RR activity of Pd-PCOF-2(Cu$_3$) (Figure 6d).

Cyclic voltammogram (CV) curves revealed that the peaks located at 0.52 V vs. RHE in the anodic scan were attributed to adsorbed active hydrogen ($^*H_{ads}$) (Figure 6e), which could be magnified for precise integration (Figure S48). The ability to generate *H could be quantitatively compared by the charges to oxidize these H* (Q_{H^*}). Pd-PCOF-1(Cu$_3$) and Pd-PCOF-2(Cu$_3$) exhibited the Q_{H^*} of 0.0099 and 0.0069 mC, respectively, which was higher than PCOF-2(Cu$_3$) (0.0015 mC), indicative of the stronger H* supply ability of Pd-porphyrin-based COFs (Figure 6f).

View Article Online
DOI: 10.1039/D6SC01645F

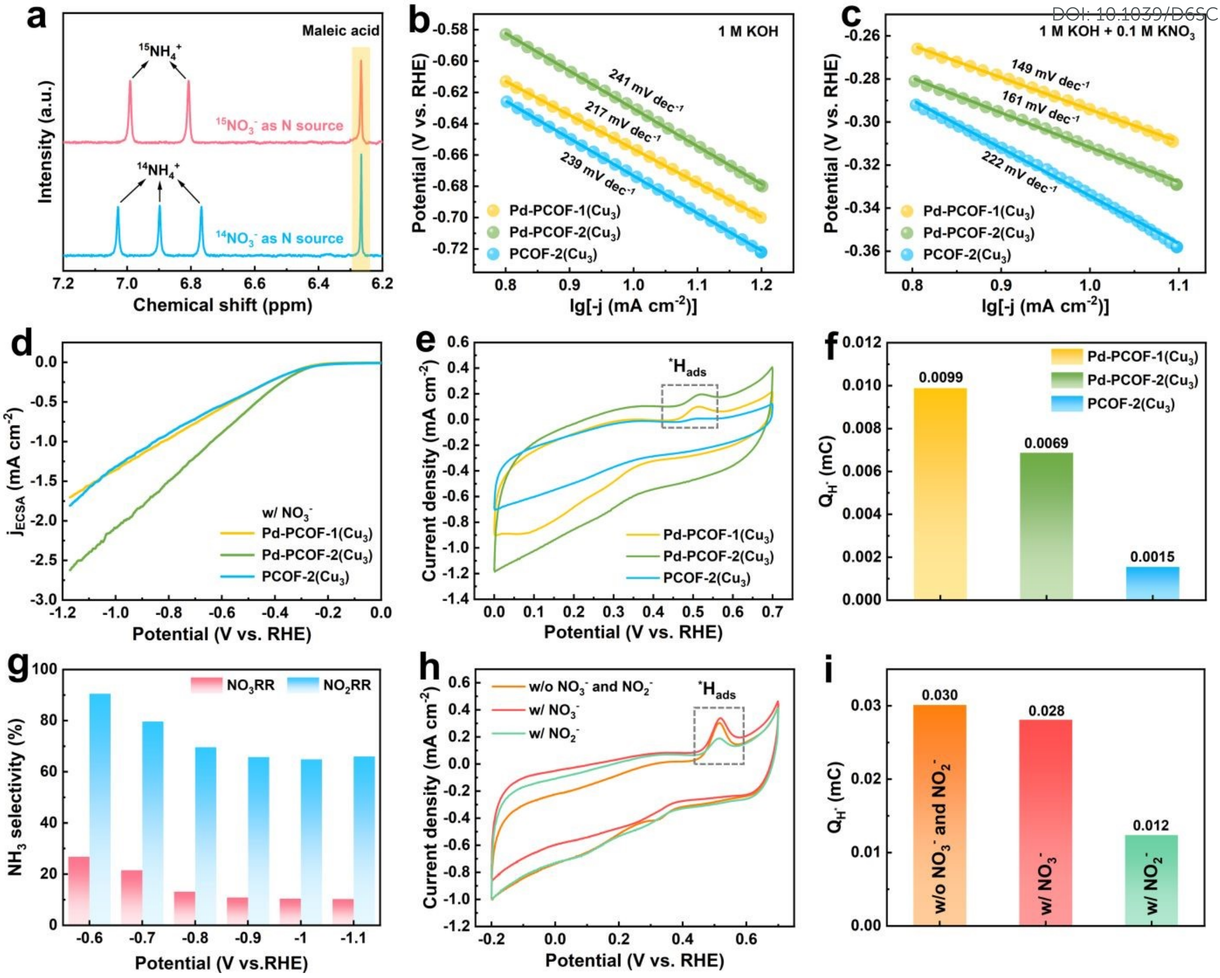

Figure 6. ^{1}H NMR spectra of the electrolytes employing $^{14}NO_3^-$ or $^{15}NO_3^-$ as N source over Pd-PCOF-2(Cu_3) (a). The Tafel plots in 1 M KOH electrolyte (b) and 1 M KOH containing 0.1 M KNO_3 electrolyte (c) of Pd-PCOF-1(Cu_3), Pd-PCOF-2(Cu_3) and PCOF-2(Cu_3). LSV curves normalized by ECSA (d). CV curves (e) and the corresponding charges of $^*H_{ads}$ (Q_{H*}) (f) of Pd-PCOF-1(Cu_3), Pd-PCOF-2(Cu_3) and PCOF-2(Cu_3) in 1 M KOH. NH_3 selectivity of Pd-EDAPP for NO_3RR and NO_2RR at different applied potentials (g). CV curves (h) and the corresponding charges of $^*H_{ads}$ (Q_{H*}) (i) of Pd-EDAPP in 1 M KOH and containing 0.1 M KNO_3 or 0.1 M KNO_2.

To investigate the synergistic effect of Cu_3-cluster and Pd-porphyrin within Pd-PCOF-2(Cu_3), electrocatalytic NO_3RR performances of $Cu_3(PyCA)_3$ and Pd-EDAPP were evaluated under the similar conditions. $Cu_3(PyCA)_3$ showed much higher current density and NH_3 FEs than Pd-EDAPP, suggesting that $Cu_3(PyCA)_3$ was the mainly active center for NO_3RR (Figures S49 and S50). $Cu_3(PyCA)_3$ displayed high NH_3 FEs (65.0~84.4%) from -0.6 to 1.1 V (vs. RHE) but negligible H_2 FEs at -0.6 V (vs. RHE). With negative potentials increasing, the H_2 FEs increased up to 26.6% at -1.1 V (vs. RHE), indicating that Cu_3 was difficult to achieve precise kinetic matching between the generation of H* and the deoxygenation process of NO_3^- (Figure S49d). For comparison, Pd-EDAPP displayed low NH_3 FEs but high H_2 FEs (56.2~84.5%) at all potentials, suggesting Pd center in porphyrin exhibited slow kinetics for the NO_3^- activation, giving rise to H_2 via the self-coupling of H* as the only rapid outlet (Figure S50e). Moreover, both $Cu_3(PyCA)_3$ and Pd-EDAPP exhibited high performance in the NO_2RR process, and the NH_3 FEs remained consistently above 60% across the entire applied potential window (Figure S51 and S52).

Catalytic results further showed that Pd-EDAPP could much more effectively activate NO_2^- than NO_3^- (Figures 6g and S53). A comparison of the LSV curves for catalytic NO_2RR demonstrated that the current density of Pd-EDAPP became much higher than that of $Cu_3(PyCA)_3$ with increasingly negative applied potential (Figure S54a). Meanwhile, the NH_3 yield rate of Pd-EDAPP was much higher than that of $Cu_3(PyCA)_3$ in NO_2RR (Figure S54b). Comparison of the consumption rate of H* on NO_2RR and NO_3RR showed that the generated H* at Pd-porphyrin showed a stronger affinity for $NO_2^–$ than $NO_3^–$ (Figures 6h, 6i and S55). These results demonstrated that during electrocatalytic nitrate reduction, Cu_3 primarily activated NO_3^- and converted a portion of NO_2^- to NH_3, while Pd-porphyrin played a synergistic role in promoting the conversion of NO_2^- to NH_3.

To uncover the detailed reaction pathway of NO_3RR, electrochemical *in situ* ATR-FTIR technique with applied

View Article Online
DOI: 10.1039/D5SC01645F

potentials from -0.6 to -1.1 V vs. RHE was employed to identify the reaction intermediates, which were generated on the surface of the Pd-PCOF-2(Cu_3) catalyst. The 3D *in situ* ATR-FTIR colormap spectra revealed distinct distributions of absorption peaks at various applied potentials (Figure 7a). The intensity of these peaks gradually increased as the applied potential became more negative. The *in situ* ATR-FTIR spectra were scrutinized over the wavenumber interval of 4000-1000 cm^{-1}, and the upward and downward bands corresponded to the formation of various nitrogen intermediates and the consumption of the corresponding reactants, respectively (Figure 7b). The pronounced absorption peaks at around 3400 and 3228 cm^{-1} were attributed to the O−H stretching of $*H_2O$ and the N−H stretching of NH_3, respectively.[38] The intensity of these peaks augmented as the potential decreased from -0.6 to -1.1 V vs. RHE, indicative of the increase in NH_3 production rate and an enhanced H_2O molecule adsorption and dissociation process. Within the 2000-1000 cm^{-1} wavenumber domain, the absorption peak at 1639 cm^{-1} was attributed to *NO and $*H_2O$.[39] The weak but discernible absorption bands at 1357 and 1100 cm^{-1} were assigned to N−O asymmetric stretching of $*NO_3$ and $*NH_2OH$, respectively.[40] Moreover, the downward band at 1241 cm^{-1} was ascribed to N−O antisymmetric stretching of $*NO_2$ and exhibited intensified strengths at more negative potentials.[41]

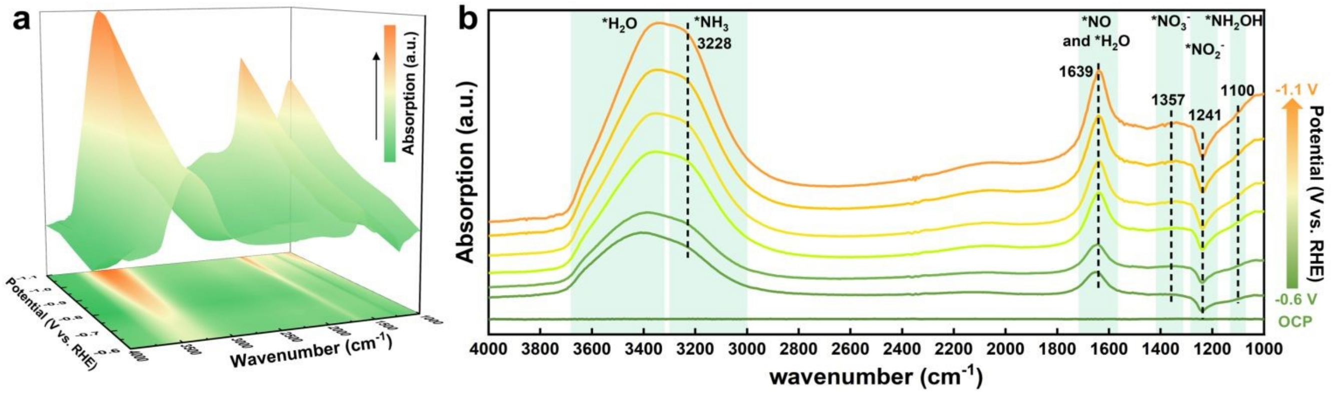

Figure 7. The 3D *in situ* ATR-FTIR colormap surface with projection of Pd-PCOF-2(Cu_3) for NO_3RR (a). Electrochemical *in situ* ATR-FTIR spectra of Pd-PCOF-2(Cu_3) for NO_3RR at different applied potentials (b).

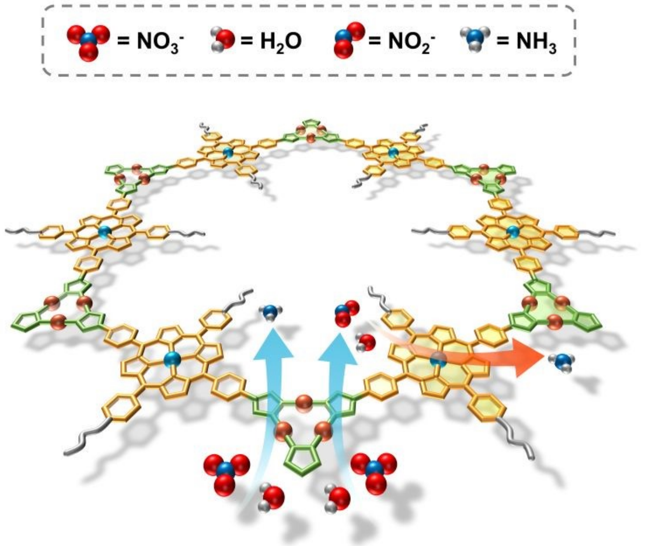

Figure 8. Schematic illustrations of catalytic mechanism for NO_3RR over Pd-PCOF-2(Cu_3).

Based on the above mechanistic studies and *in situ* ATR-FTIR spectra analysis, a reaction pathway of the NO_3RR over Pd-PCOF-2(Cu_3) might be deduced: $NO_3^- \rightarrow *NO_3 \rightarrow *NO_2 \rightarrow *NO \rightarrow *NH_2OH \rightarrow *NH_3 \rightarrow NH_3$. Consequently, NO_2^- was a critical intermediate and its excessive accumulation could lower the reaction selectivity and efficiency. The generated H* at the catalytic sites could promote the hydrogenation of NO_2^-, but its oversupply could also facilitate the competitive HER, thereby degrading the selectivity of NO_3RR. Therefore, the precise modulation of the conversion rate of NO_2^- and the supply rate of H* was crucial for enhancing both the reaction rate and the selectivity toward NH_3. In Pd-PCOF-2(Cu_3)-catalyzed NO_3RR, the Cu_3 served as the primary active sites for the initial deoxygenation NO_3^- to NO_2^- intermediate. Subsequently, Cu_3 partially hydrogenated NO_2^- to NH_3 while the unconverted NO_2^- migrated to the Pd-porphyrin for subsequent hydrogenation, which could not only effectively mitigate the accumulation of the detrimental NO_2^- intermediate but also accelerate the overall NO_3^- to NH_3 conversion kinetics. Furthermore, the tailored hydrophobic microenvironment could enable precise modulation of the H* supply for expediting the NO_2^- hydrogenation rather than HER. In short, an accelerated catalytic mechanism via synergistic tandem of bimetallic site and modulation of the hydrophobic microenvironment was elucidated (Figure 8).

Zn-NO_3^- battery. Inspired by the NO_3RR performances of Pd-PCOF-2(Cu_3), a rechargeable Zn-NO_3^- battery was constructed, which could not only generate electricity but also synthesize value-added NH_3 from NO_3^-. The Zn-NO_3^- battery was assembled with Pd-PCOF-2(Cu_3) as the cathode and Zn plate as the anode (Figure 9a). The assembled Zn-NO_3^- battery exhibited a high and stable open-circuit voltage (OCV) of approximately 1.328 V vs Zn^{2+}/Zn for up to 3600 s (Figure 9b).

View Article Online
DOI: 10.1039/D6SC01645F

The battery showed the maximum power density of 1.41 mW·cm^{-2} at a current density of 9.62 mA·cm^{-2} and the stable discharge profile over a wide range of current densities from 0.2 to 5 mA·cm^{-2} (Figure 9c and 9d), and maintained stable voltage output over 12 h during the continuous discharge-charge cycling carried out at a current density of 1 mA·cm^{-2} (Figure 9e). To verify the actual application capability of the battery, two series-connected batteries were assembled, which achieved a high OCV of approximately 2.658 V vs Zn^{2+}/Zn and successfully light up the Light Emitting Diode (LED) strip or powered a commercial electronic timer (usually driven by a commercial 1.5 V dry battery) for 24 h (Figure 9f and 9g). The NH_3 production was quantitatively analyzed after discharge under current densities of 4, 6, 8, 10 and 12 mA cm^{-2}, showing that the NH_3 generation rate increased with current density, reaching the highest value of 338.6 μg·h^{-1}·cm^{-2} (Figures 9h and S56). These results emphasized the great potential of the Pd-PCOF-2(Cu_3)-based Zn-NO_3^- battery as a stable multi-function platform in both power generation and NO_3^- conversion.

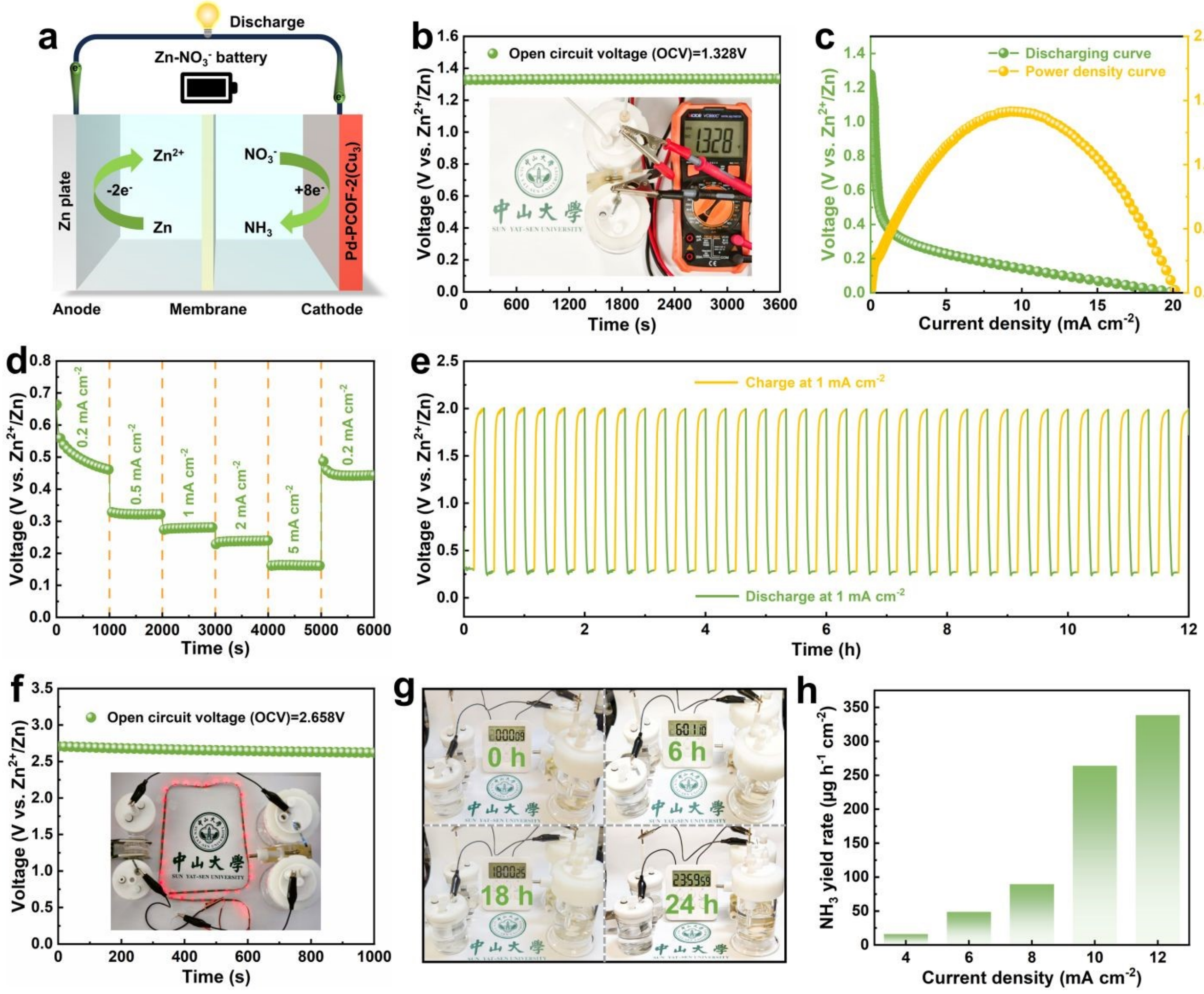

Figure 9. Schematic illustration for Zn-NO_3^- battery with Pd-PCOF-2(Cu_3) cathode (a). Open-circuit voltage (OCV) of Pd-PCOF-2(Cu_3) based Zn-NO_3^- battery (b). Polarization curve for Zn-NO_3^- battery and the resultant power density (c). Galvanostatic discharge curves at different current densities (d). Charge-discharge cycling curves of Zn-NO_3^- battery at 1 mA·cm^{-2} (e). Open-circuit voltage (OCV) of two Zn-NO_3^- batteries in series (f). Photographs of LED light strips (inside f) and electronic timer (g) powered by Zn-NO_3^- batteries. NH_3 yield rate derived from the Zn-NO_3^- battery at different discharge current densities (h).

Conclusion

In summary, an effective molecular engineering strategy was developed to construct hydrophobic bimetallic porphyrin-based COFs, integrating Pd-porphyrin and Cu_3 within the frameworks. The prepared PCOFs achieved high NO_3RR performances in alkaline electrolyte, with the Faradaic efficiency and NH_3 yield up to 94.7% and 15.09 mg·h^{-1}·cm^{-2}, respectively. A synergistic reaction mechanism was elucidated: the Cu_3 primarily facilitated NO_3^- adsorption and activation to NO_2^- and then to NH_3, while the adjacent Pd sites could assist in the hydrogenation of NO_2^- to NH_3, minimized intermediate accumulation and accelerated the overall kinetics. The pore-confined hydrophobic microenvironment played a critical role in precisely regulating the H* supply, thereby suppressing the competing HER. Overall, this work designed advanced electrocatalysts through the synergistic integration of molecular-scale hydrophobicity tuning and atomic-scale bimetallic site engineering. Further work about the synthesis of porphyrin-based COFs and their catalytic applications is on the process.

Author contributions

L.Z conceived the idea for the project and provided funding acquisition. F.L conducted the investigation, experiments, data analysis and writed original draft. H.L provided assistance in the synthesis of porphyrin ligand. C. C participated in the data analysis. L. T provided resources. D. W provided assistance in the electrocatalytic NO_3RR. C. Z provided the Materials Studio. C. S provided funding acquisition.

Conflicts of interest

The authors declare no competing financial interest.

Acknowledgements

The authors acknowledge support from the National Natural Science Foundation of China (22371306, 21821003 and 92461302), and Guangdong Basic and Applied Basic Research Foundation (2019B151502017).

References

1. X. Fu, H. Guo, D. Si, H. Zhu, Y. Lan, Y. Huang, R. Cao, *Chem. Sci*., 2025, **16**, 13503.
2. G. Wu, W. Zhang, R. Yu, Y. Yang, J. Jiang, M. Sun, A. Du, W. He, L. Dai, X. Mao, Z. Chen, Q. Qin, *Angew. Chem. Int. Ed.*, 2024, **63**, e202410251.
3. H. Lin, J. Wei, Y. Guo, Y. Li, X. Lu, C. Zhou, S. Liu, Y.-Y. Li, *Adv. Funct. Mater.*, 2024, 2409696.
4. V. Kyriakou, I. Garagounis, A. Vourros, E. Vasileiou, M. Stoukides, *Joule.*, 2020, **4**, 142-158.
5. C. Guo, J. Ran, A. Vasileff, S.-Z. Qiao, *Energy Environ. Sci.*, 2018, **11**, 45.
6. D. Liu, L. Qiao, S. Peng, H. Bai, C. Liu, W. F. Ip, K. H. Lo,H. Liu, K. W. Ng,S. Wang, X. Yang, H. Pan, *Adv. Funct. Mater.*, 2023, **33**, 2303480.
7. W. Zhong, Z. Gong, P. Chen, Q. Cao, X. Liu, Y. Chen, Z. Lin, *Chem Catalysis.*, 2025, **4**, 101060.
8. Q. Tian, X. Ye, L. Jing, W. Wang, Z. Zheng, A. Li, K. Xie, X. Huang, Q. Hu, H. Yang, X. Zhang, C. He, *Angew. Chem. Int. Ed.*, 2025, e202516919.
9. X. Zhang, X. Liu, Z.-F. Huang, L. Gan, S. Zhang, R. Jia, M. Ajmal, L Pan, C. Shi, X. Zhang, G. Yang, J.-J. Zou, *Energy Environ. Sci.,* 2024, **17**, 6717−6727.
10. S. Zheng, X. Yang, Z.-Z. Shi, H. Ding, F. Pan, J.-F. Li, *J. Am. Chem. Soc.,* 2024, **146**, 26965−26974.
11. H. Li, Z. Huang, Y. Wang, G. Hai, W.-H. Huang, C.-C. Chang, M.-H. Yeh, F. Lai, N. Zhang, T. Liu, *Angew. Chem. Int. Ed.,* 2025, **64**, e202505156.
12. X. Liu,T. Xiang, J. Liu, B. Huang, Y. Yang, X. Qu, W. Xiong, M. Cheng, G. Jiang, Y. Liu, C. Zhou, *Adv. Funct. Mater.,* 2025, e21402.
13. G. Gan, G. Hong, W. Zhang, *Adv. Funct. Mater.,* 2025, **35**, 2401472.
14. Y. Li, L. Li, S. Xu, K. Cui, T. Wang, Z. Jiang, J. Li, *Angew, Chem. Int. Ed.,* 2024, **63**, e202407810.
15. K. Liu, H. Li, M. Xie, P. Wang, Z. Jin, Y. Liu, M. Zhou, P. Li, G. Yu, *J. Am. Chem. Soc.,* 2024, **146**, 7779−7790.
16. X. Zhu, Y.-C. Wang, K. Qu, L. Song, J. Wang, Y. Gong, X. Liu, C.-F. Li, S. Yuan, Q. Lu, A.-L. Wang, *Nat. Commun.,* 2025, **16**, 5742.
17. Y. Ma, S. Liu, J. Mao, M. Sun, K. Shi, W. Li, W. Zhao, J. Shan, Y. Zhao, Z. Jiang, R. Zhang, R. Gao, W. Liu, B. Huang, G. Q. M. Lu, J. Liu, L. Wu, *Nat. Mater.,* 2026, **25**, 80–90.
18. W. Chen, Z. Sun, S. Zhen, Y. Wang, J. Sun, M. Liu, W.-J. Han, L. Lai, W. Wei, L. Zhang, W. Chen, *Adv. Funct. Mater.,* 2025, e09200.
19. W. Mei, C.-W. Chang, Z. Li, X. Wang, Y. Qie, Q. Liu, R. C. Davis, Z. Wu, Y. Yue, C. Yang, S. Li, D. Han, Q.-H. Yang, Z. Feng, Z. Weng, *Adv. Mater.,* 2025, 2507363.
20. H. Zhao, P. Liu, X. Cheng, C. Fan, J. Liu, D. Kan, Y.-Q. Wang, *Adv. Funct. Mater.,* 2025, **35**, 2425459.
21. N, Li, C. Pan, G. Lu, H. Pan, Y. Han, K. Wang, P. Jin, Q. Liu, J. Jiang, *Adv. Mater.,* 2023, 2311023.
22. Z. Zhou, T. Ma, H. Zhang, S. Chheda, H. Li, K. Wang, S. Ehrling, R. Giovine, G. Li, A. H. Alawadhi, O. M. Yaghi, *Nature.,* 2024, **635**, 96−101.
23. X. Li, S. Xia, S. Yang, X. Yang, S. Zheng, X. Xu, Y. Wang, Q. Xu, Z. Jiang, *Angew. Chem. Int. Ed.,* 2025, **64**, e202507479.
24. Y. Sun, W. Duan, J. Wang, P. Sun, Y. Zhang, Z. Li, *Chem. Sci.,* 2025,**16**, 9951-9965.
25. M. Chen, Z. Zhu, Y. Ji, X. Kong, D. Han, L. Zhai, Chem. Sci., 2025, **16**, 11669–11677.
26. H. Li, M. Cao, Z. Fu, Q. Ma, L. Zhang, R. Wang, F. Liang, T. Zhou, C. Zhang, *Chem. Sci.,* 2024, **15**, 4341–4348.
27. J. Xiong, Q. An, H. Xiang, Y. Zhou, Y. Zhang, W. Chen, B. Ren, S. Wang, H. Bai, H. Guo, X. Yang, *Chem. Sci.,* 2026, **17**, 436–447.
28. Y. Song, S. Ma, *Chem. Sci.,* 2025, **16**, 11740.
29. Z. Liang, H.-Y. Wang, H. Zheng, W. Zhang, R. Cao, *Chem. Soc. Rev.,* 2021, **50**, 2540.
30. T. Sun, Z. Wang, Y. Wang, Q. Xu, K. Wang, J. Jiang, *Angew. Chem. Int. Ed.,* 2025, **64**, e202422814.
31. J. Dong, Y. Wang, Y.-L. Lu, L. Zhang, *Chin. Chem. Lett.,* 2023, **34**, 108052.
32. S. Li, W. Deng, Y. Wang, C. Zhao, Li. Zhang, *Appl. Mater. Today.,* 2025, **47**, 102924.
33. H. Lin, Q. Mo, Y. Wang, C. Chen, L. Zhang, *Inorg. Chem.,* 2025, **64**, 2669−2680.
34. Q. Mo, C. Chen, S. Li, H. Song, L. Zhang, *Nano Res.,* 2025, **18**, 94907893.
35. Q. Mo, C. Chen, S. Li, H. Song, L. Zhang, *Small.,* 2025, **21**, 2411926.
36. Z. Zhang, M. Wang, H.-R. Xing, X. Zhou, L. Gao, S. Chen, Y. Chen, H. Xu, W. Li, S. Yuan, C.-H. Li, Z. Jin, J.-L. Zuo, *Angew. Chem. Int. Ed.,* 2025, e202505580.
37. H. Hu, R. Miao, F. Yang, F. Duan, H. Zhu, Y. Hu, M. Du, S. Lu, *Adv. Energy Mater.,* 2024, **14**, 2302608.
38. B. Zhang, Y. Chen, Z. Dai, M. Cheng, P. Feng, B. Ke, G. Zhang, *Angew. Chem. Int. Ed.,* 2025, e21064.
39. J.-Y. Fang, Q.-Z. Zheng, Y.Y. Lou, K.-M. Zhao, S.-N. Hu, G. Li, O.

View Article Online
DOI: 10.1039/D6SC01645F

Akdim, X.-Y. Huang, S.-G. Sun, *Nat. Commun.,* 2022, **13**, 7899.
40. S. Han, H. Li, T. Li, F. Chen, R. Yang, Y. Yu, B. Zhang, *Nat. Catal.,* 2023, **6**, 402–414.
41. Y. Xiao, X. Tan, B. Du, Y. Guo, W. He, H. Cui, C. Wang, *Angew. Chem. Int. Ed.,* 2024, **63**, e202408758.

View Article Online
DOI: 10.1039/D6SC01645F

Data Availability Statement

The authors confirm that the data supporting the findings of this study are available within the article and its supplementary materials.